



Title	Mesoscale simulation of fatigue behavior of concrete materials damaged by freeze-thaw cycles
Author(s)	Gong, Fuyuan; Ueda, Tamon; Wang, Yi; Zhang, Dawei; Wang, Zhao
Citation	Construction and building materials, 144, 702-716 <a href="https://doi.org/10.1016/j.conbuildmat.2017.03.207">https://doi.org/10.1016/j.conbuildmat.2017.03.207</a>
Issue Date	2017-07-15
Doc URL	<a href="http://hdl.handle.net/2115/74931">http://hdl.handle.net/2115/74931</a>
Rights	© 2017, Elsevier. Licensed under the Creative Commons Attribution-NonCommercial-NoDerivatives 4.0 International <a href="http://creativecommons.org/licenses/by-nc-nd/4.0/">http://creativecommons.org/licenses/by-nc-nd/4.0/</a>
Rights(URL)	<a href="http://creativecommons.org/licenses/by-nc-nd/4.0/">http://creativecommons.org/licenses/by-nc-nd/4.0/</a>
Type	article (author version)
File Information	Manuscript_revised.pdf



[Instructions for use](#)

# Mesoscale Simulation of Fatigue Behavior of Concrete Materials Damaged by Freeze-thaw Cycles

Fuyuan Gong<sup>1\*</sup>, Tamon Ueda<sup>2</sup>, Yi Wang<sup>3</sup>, Dawei Zhang<sup>4</sup> and Zhao Wang<sup>5</sup>

<sup>1</sup>Research Fellow, Department of Civil Engineering, The University of Tokyo, Japan. Email: gong@concrete.t.u-tokyo.ac.jp

<sup>2</sup>Professor, Lab of Engineering for Maintenance System, Faculty of Engineering, Hokkaido University, Japan

<sup>3</sup>Postdoctor, School of Civil and Transport Engineering, Guangdong University of Technology, China

<sup>4</sup>Associate Professor, College of Civil Engineering and Architecture, Zhejiang University, China

<sup>5</sup>Graduate Student, Lab of Engineering for Maintenance System, Graduate School of Engineering, Hokkaido University, Japan

## Abstract

Frost damage is a common durability problem for concrete structures in cold and wet regions, and in many cases, the frost damage is coupled with fatigue loadings such as the traffic loads on bridge decks or pavements. In this paper, to investigate the basic fatigue behavior of concrete materials affected by frost damage, a mesoscale approach based on Rigid Body Spring Method (RBSM) has been developed, of which the concrete material can be divided into three parts: mortar, coarse aggregate and interfacial transition zone (ITZ) between them. First, the cyclic constitutive laws are developed at normal and shear directions for mortar and ITZ, and verified with the existing experimental data in compression and tension fatigue. Then, several levels of frost damage are introduced by different numbers of freeze-thaw cycles (FTCs), and finally, the static tests and fatigue tests are conducted using the frost damaged concrete. The simulation results on the static strength and fatigue life show a good agreement with experimental data, and found that as the frost damage level (irreversible plastic deformation) increases, not only the static strength, but also the fatigue life at each stress level will decrease. The S-N curves of frost damaged concrete still follow a linear relationship but with bigger slopes, and the frost damaged concrete will become more ductile under fatigue loadings.

**Keywords:** concrete material; frost damage; fatigue behavior; mesoscale simulation; combined effect.

## 1. Introduction

Frost damage mechanism under freezing and thawing cycles (FTCs) is an important issue for service life evaluation of concrete structures in cold regions. Once frost damage happens, deterioration process like chloride ingress, carbonation and even the frost action itself will be largely accelerated, resulting in shorter service life. In addition, the frost action is always coupled with external loads, and the combined effect will also affect the

material degradation and structure performance significantly. If the saturation degree exceeds a critical value [1], significant damage in the porous skeleton will occur due to several kinds of pore pressures during ice formation [2-6]. This kind of internal damage will be cumulated with numbers of FTC and result in gradual degradation in material properties [7-8]. For the combined effect of FTC damage and fatigue loads, Hasan et al. [9] conducted the fatigue tests on the concrete specimens which have experienced different numbers of FTCs, and found a serious reduction of the fatigue life in compression. Although the cyclic frost action and fatigue loading have different natures, the damage of both can be reflected by the initiation and propagation of micro cracks, which will finally result in the increasing residual deformation, reduction in stiffness and strength, and so on. Therefore, it is possible to model and simulate the combined effects by the same approach.

Many concrete models are either macro model or micro model. The macro models can be directly applied to structural analysis and obtained experimentally without theoretical basis, but with less applicability once the input variables or working conditions become different. The micro models have strong theoretical bases and cover much more influential factors, but may not be convenient to study structural performances due to lack of linkage between micro and macro models. Other than above two approaches, the mesoscale approach is more general and can be applied to various kinds of damages. On one hand, the macro nonlinear mechanical behavior can be simulated by defining the constitutive laws for mortar, coarse aggregate and ITZ in mesoscale. For example, Nagai et al. [10] presented a 2D mesoscale model using RBSM, which can simulate the macroscale nonlinear properties in both compression and tension. The same mesoscale model was also extended to simulate concrete with frost damage [11], and the time-dependent degradation under fatigue loadings [12]. On the other hand, the microscale events in the porous matrix of cement paste can also be up-scaled to the mortar level, such as the pore pressures during FTCs based on poromechanics [13], and the moisture transport and chloride migration [14-15]. Some other mesoscale modeling works for concrete material can be also found [16-17]. Therefore, it would also be beneficial to adopt RBSM in mesoscale for the combined degradation problem of FTC and fatigue loadings.

In this study, based on the mesoscale RBSM, the constitutive laws under cyclic mechanical loadings are developed first, and verified with the fatigue experiments for non-FTC damaged mortar and concrete in both compression and tension. The damage effect by FTCs is also included in the above constitutive laws. For the analysis of combined effect, the FTC tests are simulated first to obtain different levels of frost damage, then using the FTC damaged concrete, static tests are conducted to obtain the residual strengths, and followed by the fatigue simulation based on each residual strength. The results are discussed in detail and compared with experimental data, which are found in a satisfactory agreement.

## **2. Method of Analysis**

### **2.1 Concept of RBSM**

The RBSM is a discrete numerical analysis method, which was first developed by Kawai [18]. Unlike the continuum methods such as Finite Element Method or Finite Difference Method, RBSM is a more proper way to simulate splitting and cracking in cement-based materials like mortar and concrete. Also, compared to other discrete method like Distinct Element Method, RBSM is more suitable for small deformation and tiny cracks which are often seen in concrete structures.

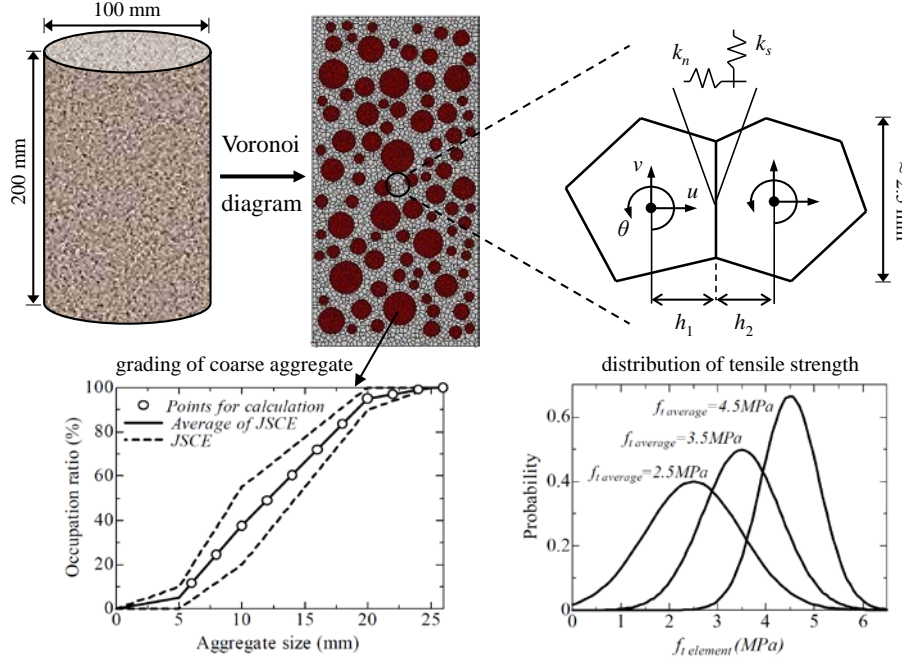


Fig. 1 Basic concept of RBSM analysis [10]

The concrete to be simulated is divided into polyhedron elements, and the mesh is arranged randomly using a Voronoi diagram. Each Voronoi cell represents a mortar or aggregate element in the model. For two adjacent elements, there are two springs connecting them: normal spring and shear spring, which are placed at the boundary of the elements (see Fig. 1). Each element has two translational and one rotational degree of freedom at the centroid. The normal and shear stiffness are calculated by assuming a plane stress condition as follows [10]:

$$\begin{aligned} k_n &= E / (1 - \nu^2) \\ k_s &= E / (1 + \nu) \end{aligned} \quad (1)$$

where  $k_n$  and  $k_s$  are the stiffness of normal and shear spring;  $E$  and  $\nu$  are the elastic modulus and Poisson's ratio of the element (either mortar or aggregate), respectively. In case of the springs on the mortar-aggregate interface, the stiffness is given as a weighted average of mortar and aggregate element:

$$\begin{aligned} k_n &= (k_{n1}h_1 + k_{n2}h_2) / (h_1 + h_2) \\ k_s &= (k_{s1}h_1 + k_{s2}h_2) / (h_1 + h_2) \end{aligned} \quad (2)$$

where the subscripts 1 and 2 represent the mortar and aggregate elements respectively, and  $h$  is the length of the

perpendicular line from the centroid of element to the boundary. The stress-strain relationship of the normal spring will adopt a linear tension-softening curve, and a normal distribution was assumed for the tensile strength to increase the heterogeneous performance as [10]:

$$f(f_t) = \frac{1}{\sqrt{2\pi}s} \exp\left[-\frac{(f_t - \mu)^2}{2s^2}\right] \quad (3)$$

$$s = -0.2\mu + 1.5$$

where  $f_t$  is the tensile strength of the element, and for  $f_t < 0$ , set  $f_t = 0$ ;  $\mu$  is the average value of  $f_t$ ; and  $s$  is the standard derivation. For the shear spring of porous body, the following criterion is adopted [10]:

$$\tau_{\max} = \pm \left( 0.11 f_t^3 (-\sigma + f_t)^{0.6} + f_t \right) \quad (\sigma \leq f_t) \quad (4)$$

where  $\sigma$  is the normal stress. And for the interface between mortar and aggregate, the shear spring criterion is as follows:

$$\tau_{\max} = \pm (-\sigma \tan \varphi + c_i) \quad (5)$$

where  $\varphi$  and  $c_i$  are constant values. For the shear springs of both mortar and ITZ, the ideal plastic performance is assumed when the local shear strain is small [10], however, if the shear sliding becomes so big that the attached length of two elements is significantly reduced, the shear transfer will also decrease linearly as:

$$\begin{aligned} \tau_{\max}' &= \tau_{\max} (1 - \delta_s / l_{elem}) \\ k_s' &= k_s (1 - \delta_s / l_{elem}) \end{aligned} \quad (6)$$

where  $\delta_s$  is the sliding distance and  $l_{elem}$  is the length of boundary between two elements. It can be imaged that the local shear strain in mesoscale could be several orders larger than the averaged shear strain in macroscale when failure happens, thus the above formulation can still guarantee a shear softening behavior in macroscale.

The tensile cracking and shear sliding will also interact with each other for both mortar elements and ITZ. The concept of mesoscale analysis is that the constitutive laws should be as simple as possible to simulate the complicated macroscale mechanical behavior. Considering that the tension stress transfer capability may be reduced with damage induced by sliding at the same location, the tension softening stress is assumed reducing linearly with the amount of shear sliding between two adjacent elements:

$$\begin{aligned} f_t' &= f_t (1 - \delta_s / l_{elem}) \\ k_n' &= k_n (1 - \delta_s / l_{elem}) \end{aligned} \quad (7)$$

Similarly, the shear strength ( $\tau_{\max}''$ ) and stiffness ( $k_s''$ ) also can be affected by the tensile cracking, and a linear relation is assumed:

$$\begin{aligned} \tau_{\max}'' &= \tau_{\max}' (1 - w / w_{\max}) \\ k_s'' &= k_s' (1 - w / w_{\max}) \end{aligned} \quad (8)$$

where  $w$  is the crack width in normal direction and  $w_{max}$  is the maximum crack width which tensile and shear transfer can happen. The above coupling effect has been verified by the uniaxial compression tests and biaxial compression-tension tests [10]. The mathematical solution of the RSBM is briefly summarized in Appendix A.

## 2.2 Cyclic constitutive laws

In fatigue test, the applied stress is less than macroscale strength, and inducing stresses in mesoscale whose average is less than the average strength of all springs. Since the normal distribution of tensile strength was assumed for normal springs (the shear criterion will also be affected according to Eq. (4)), a part of springs will still break. Then the broken springs will lose capacity gradually and result in new breaking springs. After a period of damage cumulating, the material will get failure finally. The constitutive model for fatigue and creep based on RBSM has been studied by Matsumoto et al. [12] and modified later [19]. Matsumoto et al.'s model contains four kinds of mechanical components in both normal and shear springs: the elastic, plastic, visco-elastic and visco-plastic component, which can simulate both the fatigue damage and time dependent creep from the very basic constitutive laws. On the contrary, for FTC induced damage, both the previous mesoscale experiments [20-21] and constitutive modeling [8,13] were mainly focusing on the time-independent deformation and damage (only contains elastic and plastic components), but the creep effect during FTCs is still not clear. Therefore, to combine the fatigue and FTC damage into the same constitutive laws, and also to make the mesoscale model simpler, the combined effects are formulated only with elastic and plastic components, while the creep strain is calculated separately for each normal spring based on the existing models [22-23].

### 2.2.1 Cyclic normal and shear deterioration in mortar and ITZ

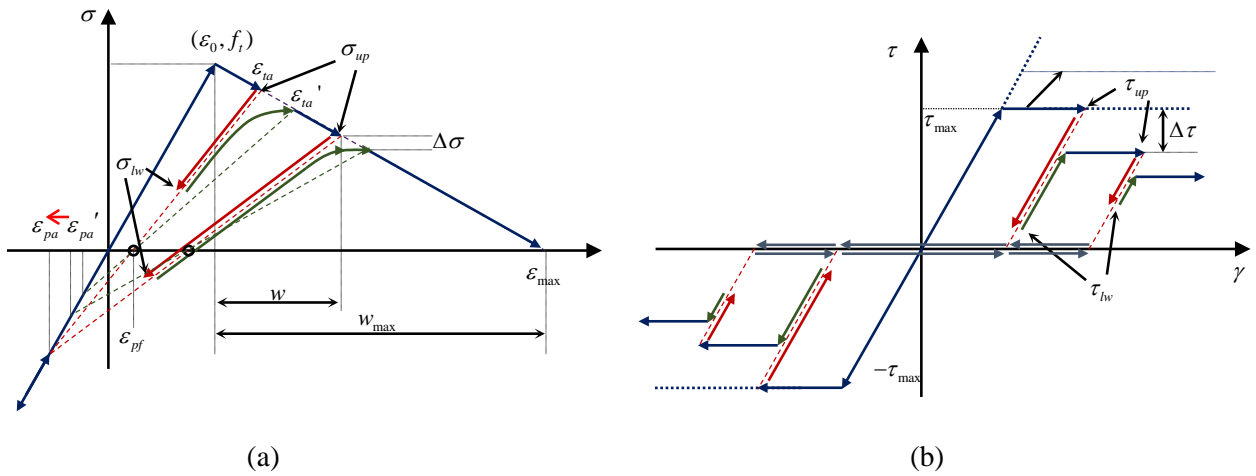


Fig. 2 Constitutive Laws under cyclic loading (a) Normal spring (b) Shear spring

The cyclic constitutive laws of normal and shear springs are shown in Fig. 2. The nonlinear stress-strain curve of normal spring was originally defined in Nagai et al. [10], and followed by Ueda et al. [11] which considered the irreversible tensile plastic strain ( $\varepsilon_{pf}$ ) by introducing one constant strain ( $\varepsilon_{pa} = 400\mu$ ) at the compression branch. For fatigue simulation, the unloading curves (red line) and reloading curves (green line) should not be exactly the same, so that the cyclic degradation can be taken into consideration. According to Fig. 2 (a), once the tensile strength ( $f_t$ ), initial stiffness ( $f_t / \varepsilon_0$ ) and the maximum tensile strain at zero stress ( $\varepsilon_{\max}$ ) are known, then when the peak tensile strain ( $\varepsilon_{ta}$ ) reaches the plastic region, the irreversible plastic tensile strain ( $\varepsilon_{pf}$ ) during unloading would be [8]:

$$\varepsilon_{pf} = \frac{\varepsilon_{\max}(\varepsilon_{ta} - \varepsilon_0)}{(\varepsilon_0 + \varepsilon_{pa})(\varepsilon_{\max} - \varepsilon_0) - \varepsilon_0(\varepsilon_{ta} - \varepsilon_0)} \varepsilon_{pa} \quad (9)$$

where  $\varepsilon_0$  is the strain at the tensile strength. During the cyclic unloading-reloading process, small damage will be generated and cumulated gradually, thus in each loading cycle, the reloading curve cannot go back to the peak point of last cycle ( $\sigma_{up}$ ,  $\varepsilon_{ta}$ ), but will be slightly softened to  $\varepsilon_{ta}'$ , whose value can be determined by introducing another  $\varepsilon_{pa}'$  for the reloading curve, which is:

$$\varepsilon_{ta}' = \frac{(\varepsilon_{pa}' + \varepsilon_{pf})\varepsilon_0\varepsilon_{\max} + (\varepsilon_{\max} - \varepsilon_0)\varepsilon_{pf}\varepsilon_{pa}}{\varepsilon_{pa}\varepsilon_{\max} + \varepsilon_{pf}\varepsilon_0} \quad (10)$$

where degradation parameter  $\varepsilon_{pa}'$  should depend on the stress level of previous cycle:

$$\varepsilon_{pa}' = \varepsilon_{pa} \cdot \left( 1 + c_{nm} \left( \frac{\sigma_{up}}{f_t} \right)^{\alpha_m} \left( \frac{\sigma_{up} - \sigma_{lw}}{f_t} \right) \right)^{-1} \quad (11)$$

where  $\sigma_{up}$  and  $\sigma_{lw}$  are the upper and lower normal stress of previous cycle,  $c_{nm}$  and  $\alpha_m$  are parameters for mortar which reflect the effect of unloading and reloading on the stress reduction, and need to be calibrated. Then during every unloading process,  $\varepsilon_{pa} = 400\mu$  will be used to achieve the new irreversible plastic strain  $\varepsilon_{pf}$ , while during the reloading process,  $\varepsilon_{pa}'$  will be adopted. From Eq. (11),  $\varepsilon_{pa}'$  is a changing value depending on the stress condition ( $\sigma_{up}$  and  $\sigma_{lw}$ ) of previous cycle. As the plastic strain increases ( $\sigma_{up}$  decreases),  $\varepsilon_{pa}'$  will move to  $\varepsilon_{pa}$  gradually and the cyclic degradation will also become smaller. By doing so, the gradual degradation process can be simulated from the mesoscale constitutive laws smoothly.

For the shear spring of mortar element, similar stress drop is introduced to reflect the degradation during cyclic loadings (Fig. 2 (b)). The maximum shear capacity (shear criterion) will be affected by both the crack width in normal spring and the unloading and reloading history of the shear spring itself, which is:

$$\begin{aligned} \tau_{\max} &= \pm \left[ 0.11 f_t^3 (f_t - \sigma)^{0.6} + f_t \right] \times f_1 \times f_2 \\ f_1 &= 1 - w / w_{\max} \\ f_2 &= \prod_N \left( 1 - c_{sm} \left( \frac{\tau_{up}}{f_t} \right)^{\beta_m} \left( \frac{\tau_{up} - \tau_{lw}}{f_t} \right) \right) \end{aligned} \quad (12)$$

where  $f_1$  is the reduction factor due to the crack opening in normal direction and  $f_2$  reflects the effect of cyclic shear stress, which will be cumulated with the fatigue cycles ( $N$ ).  $w=(h_1+h_2)(\varepsilon-\varepsilon_0)$  is the crack width after the tensile strain exceeds the critical strain ( $\varepsilon_0$ ) at the tensile strength ( $f_t$ ), and  $w_{\max}=(h_1+h_2)(\varepsilon_{\max}-\varepsilon_0)$  is the maximum crack width, which is usually 0.03mm for mesoscale analysis [10].  $c_{sm}$  and  $\beta_m$  are the parameters of mortar reflecting the continuous degradation of the shear spring by cyclic unloading and reloading.  $\tau_{up}$  and  $\tau_{lw}$  are the upper and lower stresses in the shear springs. The parameters for mortar after calibration are:

$$\begin{aligned} c_{nm} &= 8.0 \\ c_{sm} &= 1.0 \times 10^{-8} \\ \alpha_m &= 14.0 \\ \beta_m &= 6.0 \end{aligned} \quad (13)$$

For the concrete, the ITZ must be taken into consideration. Although the properties of the ITZ are usually weaker than the mortar, the general characteristics of the degradation at interface should be similar with the mortar. Therefore, similar idea is applied on the interface, then, for the normal spring of ITZ:

$$\varepsilon_{pa}' = \varepsilon_{pa} \cdot \left( 1 + c_{ni} \left( \frac{\sigma_{up}}{f_t} \right)^{\alpha_i} \left( \frac{\sigma_{up} - \sigma_{lw}}{f_t} \right) \right)^{-1} \quad (14)$$

And for the shear spring of ITZ:

$$\begin{aligned} \tau_{\max} &= \pm(-\sigma \tan \varphi + c_i) \times f_1 \times f_2 \\ f_1 &= 1 - w / w_{\max} \\ f_2 &= \prod_N \left( 1 - c_{si} \left( \frac{\tau_{up}}{f_t} \right)^{\beta_i} \left( \frac{\tau_{up} - \tau_{lw}}{f_t} \right) \right) \end{aligned} \quad (15)$$

where  $w_{\max}$  for ITZ is set as 0.01mm [10], the parameters  $c_{ni}$ ,  $\alpha_i$ ,  $c_{si}$  and  $\beta_i$  have the same physical meaning with the mortar element, but the values should be different to reflect different degradation speed under cyclic loads, which are chosen as:

$$\begin{aligned} c_{ni} &= 20.0 \\ c_{si} &= 3.0 \times 10^{-13} \\ \alpha_i &= 9.0 \\ \beta_i &= 9.0 \end{aligned} \quad (16)$$

## 2.2.2 Basic creep and fatigue creep in mortar and ITZ

During the fatigue test, the duration is usually long enough to have obvious creep deformation. The creep occurs at all stress levels and, within the service stress range, is linearly dependent on the stress if the pore water content is constant. There are several models to estimate the creep strain under sustained loads, such as the B3



Model [22]. In addition, Bazant and Hubler also developed a theoretical model for the creep under fatigue loadings based on Paris law [23], in which the total creep strain is:

$$\varepsilon_N = J_{tot} \sigma_{mean} \quad (17)$$

where  $\varepsilon_N$  is the total creep strain after  $N$  cycles;  $J_{tot}$  is the total material compliance (the creep strain caused by per unit of stress);  $\sigma_{mean}=0.5(\sigma_{max}+\sigma_{min})$  is the mean stress of the fatigue loading. The total compliance is composed by two parts:

$$J_{tot} = J(t, t_0) + J_N \quad (18)$$

where  $J(t, t_0)$  is the compliance for ordinary creep based on the B3 Model [22];  $J_N$  is the compliance for the cyclic effect of fatigue. If excluding the elastic response during the fatigue test, and also moisture content is assumed constant, then  $J(t, t_0)$  would be as follows according to the B3 Model:

$$J(t, t_0) = q_2 Q(t, t_0) + q_3 \ln[1 + (t - t_0)^n] + q_4 \ln\left(\frac{t}{t_0}\right) \quad (19)$$

where  $q_2$ ,  $q_3$  and  $q_4$  represent the ageing viscoelastic compliance, non-ageing viscoelastic compliance, and flow compliance, respectively [22]; and  $Q(t, t_0)$  is a binomial integral which cannot be expressed analytically, whose values are shown in previous paper [22];  $n$  is a constant which equals to 0.1;  $t_0$  is the age when the loads are applied (in days);  $t$  is the current time (in days). The determination of those parameters follows:

$$\begin{cases} q_2 = 185.4c^{0.5}f_c^{-0.9} \\ q_3 = 0.29(w/c)^4 q_2 \\ q_4 = 20.4(a/c)^{-0.7} \end{cases} \quad (20)$$

where  $w$ ,  $c$  and  $a$  are the content ( $\text{kg}/\text{m}^3$ ) of water, cement and aggregates respectively.

The cyclic creep during fatigue is also called fatigue creep, which is a long-term deformation due to cyclic load in addition to the static creep, and given its expression as [23]:

$$J_N = C_t \left( \frac{\Delta\sigma}{f_c} \right)^\alpha N \quad (21)$$

where  $C_t$  is constant which is chosen as  $6.67 \times 10^{-3}$  (micron/MPa) [23];  $N$  is the number of fatigue cycles;  $\alpha$  is a constant which equals to 4 [23];  $\Delta\sigma$  is the amplitude of the fatigue loads. It should be noticed that the above empirical formulas in B3 model and fatigue creep model are all calibrated based on concrete material, while in the mesoscale RBSM, the creep is only considered in mortar and ITZ. For the creep phenomenon in concrete materials, the viscous flow of capillary and gel water under permanent loadings has been deemed as the main mechanism [24], thus a simple relation for creep has been built between cement and concrete containing aggregates [25]:

$$\varepsilon_c / \varepsilon_p = (1 - g)^{1.9} \quad (22)$$

where  $\varepsilon_c$  and  $\varepsilon_p$  are the creep strain of concrete and cement paste respectively;  $g$  is the volume ratio of aggregates. Based on the creep mechanism, also considering that in both B3 model and Neville's formula, there is no strict difference between coarse aggregate (gravel) and fine aggregate (sand), thus in this paper, the B3 model is still applicable if adopting the mix proportion of mortar. The creep in ITZ may not be ignored because its porosity is even larger than cement paste, but in the RBSM, only the ITZ of coarse aggregates are considered separately, while the ITZ of sands are already averaged into the mortar element. Thus, the creep deformation of ITZ around coarse aggregates has little contribution to the total creep deformation due to its limited volume ratio. However, the creep may still have some effects on the mechanical properties of ITZ, thus, the same creep model is applied on the normal springs at ITZ for a simple consideration of the damage effect. Then, if taking  $w=310$ ,  $c=620$  and  $a=1240$  (sand) for mortar sample as in the literature [19], with different loading frequency, the basic creep ( $J(t, t_0)$ ) and the fatigue creep ( $J_N$ ) can be estimated as in Fig. 3 (a) (the horizontal axis means loading cycles). It can be seen that the basic creep is almost linear to the logarithm value of cycles while the fatigue creep is linear to the numbers of loading cycles. Fig. 3 (b) shows the total compliance for different stress levels. It can be seen that for the low cycle fatigue, the fatigue creep is not significant while the main creep deformation comes from the basic creep. But for the high cycle fatigue, the fatigue creep becomes obvious and the higher stress level is, the bigger creep compliance will be.

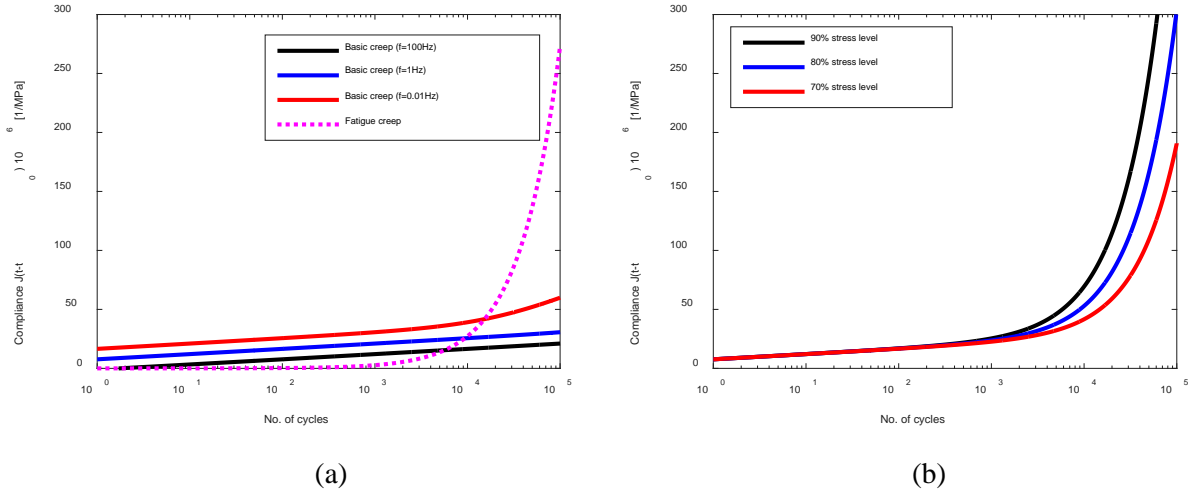


Fig. 3 The estimated creep compliance during fatigue test (a) Under different loading frequency (80% stress level)  
(b) Under different stress level ( $f=1\text{Hz}$ )

The above model can be directly applied to the single fatigue problem, but when the FTC and fatigue loads happens together, the stress level on the concrete skeleton may vary with time, thus a differentiation form of Eq. (19) with respect to time is needed [22]:

$$\frac{\partial J(t, t_0)}{\partial t} = \frac{n(q_2 t^{-m} + q_3)}{(t - t_0) + (t - t_0)^{1-n}} + \frac{q_4}{t}, \quad m = 0.5, n = 0.1 \quad (23)$$

Here the effective stress on the porous skeleton caused by FTC has been formulated from the pore pressures based on poromechanics, which will be briefly summarized in the next section. As a simple coupling of FTC and fatigue loading in this study, the two process happens independently in sequence (FTC first and followed by fatigue), the cyclic FTC stress can be similarly regarded as a fatigue load but with different frequency and amplitude. When the FTC and fatigue loading are applied to concrete simultaneously, considering the big difference in the time scale, the total stress can still be regarded as a high-frequency fatigue load whose mean value changes periodically at a low-frequency, and this type of coupling will be investigated in future. Therefore, in this study, the total creep strain under sequential FTC and fatigue loading will be:

$$\varepsilon_N = \sigma(t) \int \frac{\partial J(t, t_0)}{\partial t} dt + \sigma_{mean} C_t \left( \frac{\Delta \sigma}{f_c} \right)^\alpha N \quad (24)$$

where  $\sigma(t)$  is the real-time stress either by FTC or fatigue loading;  $\sigma_{mean}$  and  $N$  are the mean stress and number of cycles in either FTC or fatigue process. Finally, in the RBSM simulation, the total creep compliance will be introduced to each normal spring according to their particular stress conditions (stress level, amplitude, history etc.).

### 2.3 Nonlinear model with ice

The nonlinear constitutive laws with the effect of ice expansion has been developed in previous study [13]. In which the internal stress due to ice formation will linearly decrease when the expansion of porous skeleton becomes bigger (Fig. 4 (a)), and finally the ice and liquid water in pores will reach a mechanical equilibrium with the porous material (the intersection point of two constitutive curves). During this process, the initial effective stress ( $\sigma_0$ ) is generated inside the spring of ice and water (like in a pre-compressed condition). This model can describe the real physical process well but is not convenient for the numerical simulation, especially when external load (mechanical load) is also applied outside of two springs. However, it can be proved mathematically that the final states of spring for porous body are the same when  $\sigma_0$  is directly applied outside on two springs (Fig. 4 (b)). Then the spring of ice-water will only act as an aided tool to get the correct status of the porous body, but with less physical meaning. Since the main target is to find the deterioration of the porous body, this transformation has no effect on the porous material and on the contrary, the internal effective stress can be treated as an ordinary external load.

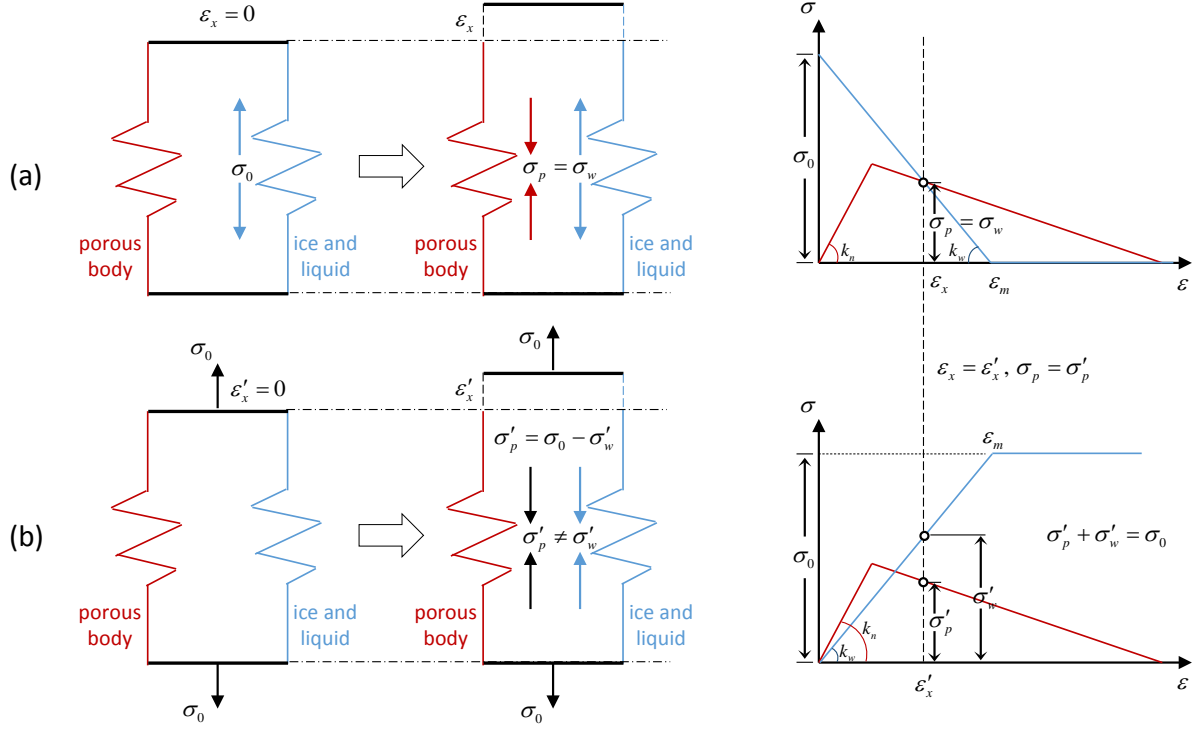


Fig. 4 Parallel model for normal spring with ice volume expansion (a) Stress generated in ice system (b) Stress applied on both porous body and ice system [13]

The normal spring of porous body in Fig. 4 exactly follows the constitutive model developed in previous sections, while for the spring of ice and liquid, the following linear behavior has been proposed [13]:

$$0.09\phi\psi_C = \left( \frac{\phi\psi_C}{K_C} + \frac{\phi\psi_L}{K_L} \right) \cdot \frac{\sigma_w}{b} + 3\varepsilon_x \quad (25)$$

where  $\phi$  is the void ratio of mortar;  $\psi_C$  and  $\psi_L$  are the volume fraction of ice and unfrozen water in the total pore space, which can be either empirically estimated [26] or regressed from experiments [27];  $K_C$  and  $K_L$  are the bulk moduli of ice and water;  $\varepsilon_x$  is the one-dimensional expansion of porous skeleton;  $b$  is the Biot coefficient which reflects the effective stress ( $\sigma_w$ ) on the porous skeleton caused by the pore pressure ( $p_h$ ), that is:  $\sigma_w = b \cdot p_h$ . The Biot coefficient can be approximately equal to  $2\phi/(1+\phi)$  [27]. Actually Eq. (25) expresses the linear curve in Fig. 4, and it can also be seen that the initial stress ( $\sigma_0$ ) and the stiffness ( $k_w$ ) of ice-liquid spring are:

$$\sigma_0 = b \cdot 0.09\phi\psi_C / \left( \frac{\phi\psi_C}{K_C} + \frac{\phi\psi_L}{K_L} \right) \quad (26)$$

$$k_w = \frac{3b}{\phi[\psi_C / K_C + \psi_L / K_L]} \quad (27)$$

Then the ice expansion problem can be solved by simply adding another stiffness matrix:

$$1 \quad [K_p + K_w]\{u\} = \{F_0\} \quad (28)$$

2 where  $[K_p]$  and  $[K_w]$  are the stiffness matrix of the porous body and ice-water system, respectively. And the load  
3 boundary condition  $\{F_0\}$  can be calculated using  $\{\sigma_0\}$ :

$$4 \quad \{F_0\} = [B]^T \{\sigma_0\} \quad (29)$$

5 where  $[B]$  is the deformation matrix in RBSM analysis. Since the internal effective stress is a volume stress, it can  
6 be considered only applied on the normal spring, then finally the stiffness matrix would be:

$$7 \quad \mathbf{D} = \begin{bmatrix} k_n + k_w & 0 \\ 0 & k_s \end{bmatrix} \quad (30)$$

### 8 **3. Simulation Model**

#### 9 **3.1 Model size and boundary conditions**

10 The model and boundary condition for the fatigue tests and the combined tests are shown in Fig. 5, in which  
11 the mortar prism will be used to verify the fatigue life that is predicted from the simplified fatigue constitutive  
12 laws without FTC damage, and compared with previous simulations [19] and experiments [29]. The mesh size  
13 and convergence criterion are chosen considering the balance between calculating efficiency and accuracy, which  
14 is briefly discussed in Appendix B. Then the pure fatigue model will be extended from mortar to concrete, and the  
15 fatigue life of concrete will be compared with experimental data. Circular coarse aggregates are distributed  
16 randomly according to the size distribution specified in JSCE standard [28], with a maximum diameter of 20mm.  
17 The volume of aggregates is around 40% of the total volume of the models. There is a layer of boundary elements  
18 (loading plate with zero thickness) between the applied loads and the mortar [19]. For the fixed boundary, all the  
19 degrees of freedom ( $x$ ,  $y$  and  $\theta$ ) are fixed; while for the loading plates, only  $x$  and  $\theta$  are fixed. After verifying the  
20 pure fatigue simulation of mortar and concrete, the combined FTC and fatigue test will be simulated on the  
21 concrete prism.

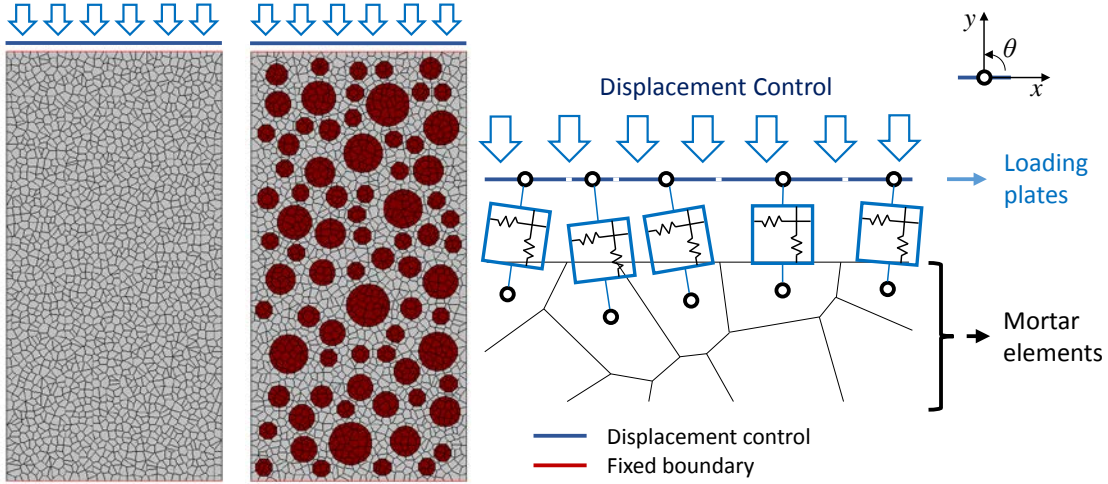


Fig. 5 The model and boundaries for fatigue test and combined test with FTC (Mortar prism: 200mm×100mm×100mm, 1859 elements; Concrete prism: 200mm×100mm×100mm, 2566 elements)

### 3.2 Material properties

The determination process of input material properties will be based on literature [10], in which the compressive strength (Eq. (19)), elastic modulus (Eq. (20)) and the tensile strength (Eq. (21)) are given as follows:

$$f'_{cm} = 21.3c/w - 10.6 \quad (31)$$

$$E_m = 1000(7.7 \ln f'_{cm} - 5.5) \quad (32)$$

$$f_{tp} = 1.4 \ln f'_{cm} - 1.5 \quad (33)$$

where  $c/w$  is the inverse value of  $w/c$  ratio,  $f'_{cm}$  is the static compressive strength of mortar (MPa),  $E_m$  is the elastic modulus of mortar (MPa) and  $f_{tp}$  is the pure tensile strength of mortar (MPa). The properties of interface are regressed as follows [10]:

$$f_{ti} = -1.44w/c + 2.3 \quad (34)$$

$$c_i = -2.6w/c + 3.9 \quad (35)$$

where  $f_{ti}$  is the tensile strength of mortar-aggregate interface (MPa),  $c_i$  is the constant in Eq. (5) (MPa). The elastic modulus of coarse aggregate is set as 50GPa; the Poisson's ratio of mortar and aggregates are 0.18 and 0.25; and the constant  $\varphi$  in Eq. (5) is chosen as  $35^\circ$  [10]. Table 1 shows the input material properties of the mortar and concrete in this simulation, and also the simulated static compressive and tensile strengths of the undamaged mortar and concrete are shown in Fig. 6.

Table 1 The material properties in the FTC and fatigue simulation

ID	$w/c$	$f'_{cm}$ (MPa)	$E_m$ (GPa)	$f_{tp}$ (MPa)	$\varphi$	$c_i$ (MPa)	$f_{ti}$ (MPa)	$f_c$ (MPa)	$f_t$ (MPa)
M1								36.60	3.49
M2	0.47	35.0	21.876	3.48	-	-	-	37.80	3.42
M3								35.93	3.55
C1								28.48	2.53
C2	0.47	35.0	21.876	3.48	35°	2.69	1.63	29.85	2.43
C3								30.04	2.51

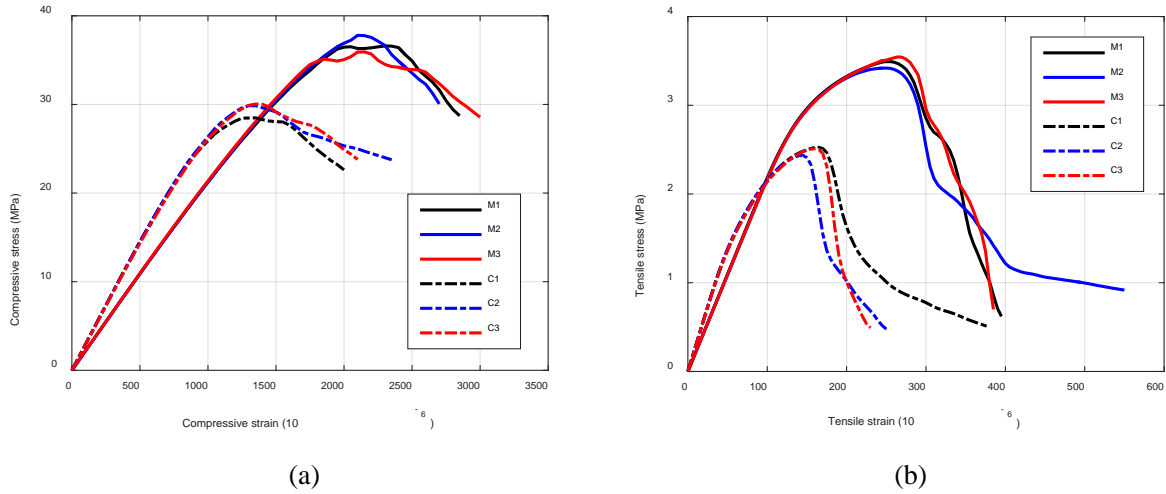


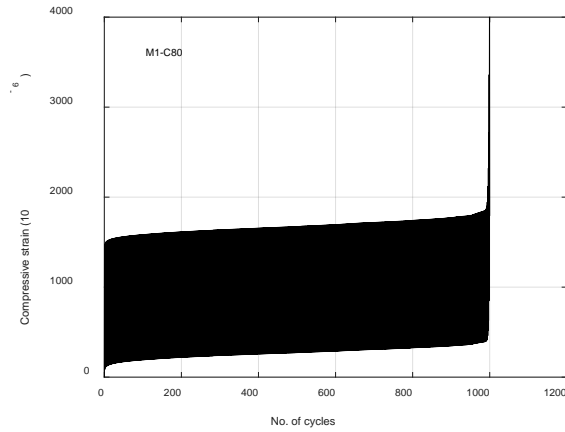
Fig. 6 The static strengths of mortar and concrete without FTC damage (Left: compressive. Right: tensile)

## 4. Results and Discussions

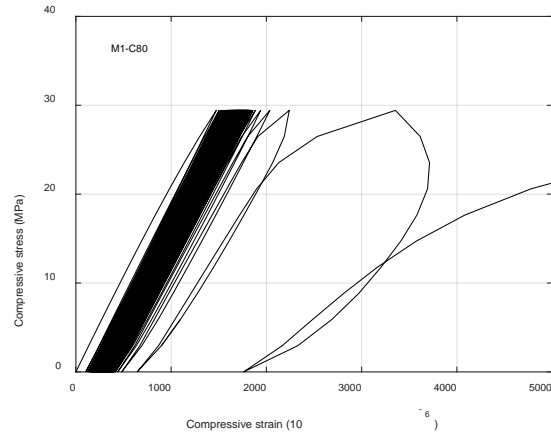
### 4.1 Pure fatigue for mortar and concrete

First, the pure fatigue tests are conducted on the mortar prism. The global strain is defined as the average strain from the top to the bottom surface, and the global stress is the average stress on the loading (top) surface. Then, the global strain history and the global stress-strain curves in compressive and tensile fatigue are shown in Fig. 7. In which “M1-C80” means mortar sample 1 under a stress level of 80% of the compressive strength, while “T” represents tensile strength accordingly. For the compressive fatigue of mortar, as the number of fatigue cycles increases, there is an increment in the maximum strain and residual strain until it reaches the very end of fatigue life. According to the mechanical model in this paper, the residual plastic strain is only introduced to the normal spring for the tensile part. However, for the compressive failure of mortar with the boundaries fixed in the

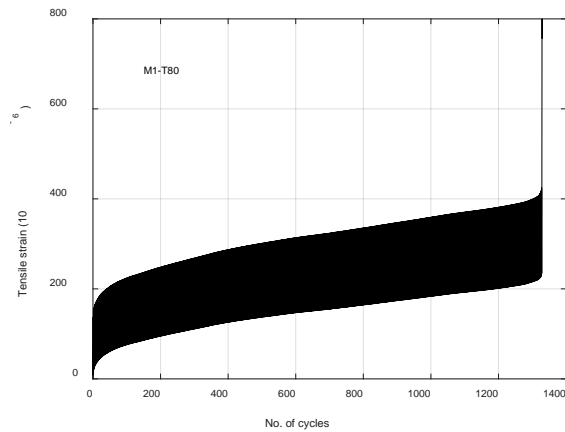
1 horizontal direction, the final failure is mainly controlled by the shear criterion. Therefore, although the damage  
 2 will cumulate in the shear springs gradually during unloading and reloading, the residual deformation due to  
 3 damage along the vertical axis will still not be obvious compared to the creep, until the very end of fatigue life.  
 4 Thus, the residual deformation in the analysis is mainly because of the creep effect. On the contrary, the tensile  
 5 failure is mainly depending on the normal spring, so the gradual increasing maximum strain and residual strain  
 6 contains both creep deformation and the crack opening.



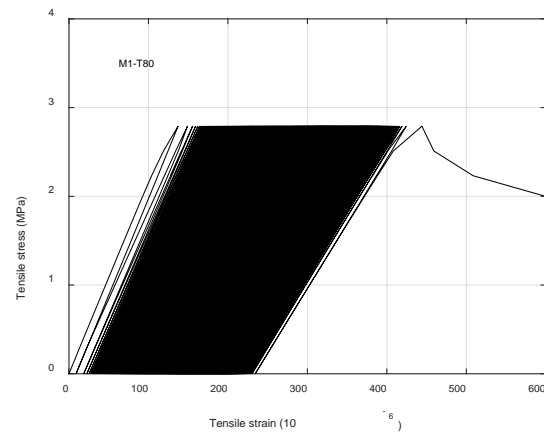
(a)



(b)



(c)

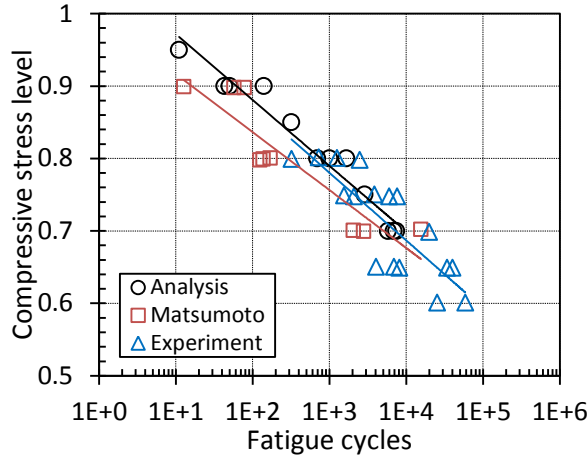


(d)

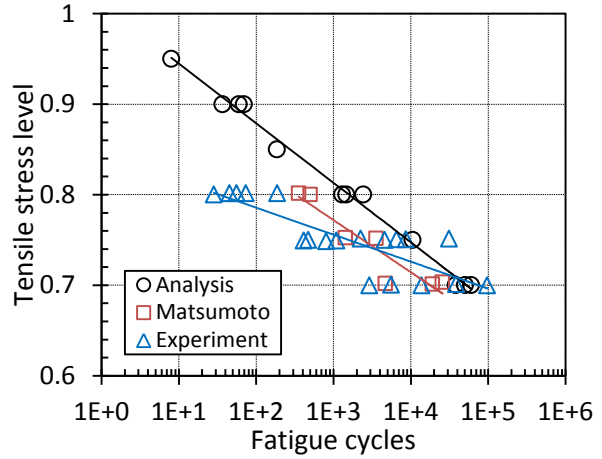
Fig. 7 The global strain history and the global stress-strain curves of the mortar in compressive and tensile fatigue.

(a) Strain history in 80% compression (b) Stress-strain curve in 80% compression  
 (c) Strain history in 80% tension (d) Stress-strain curve in 80% tension





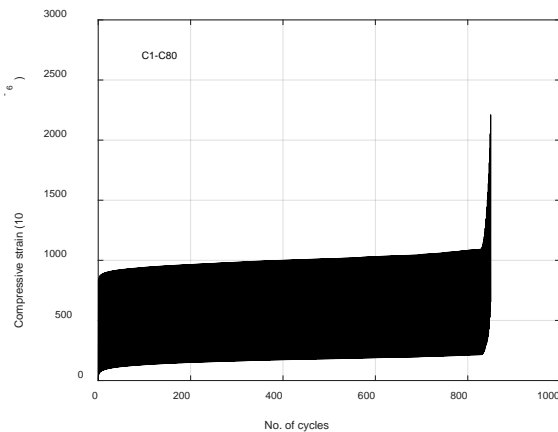
(a)



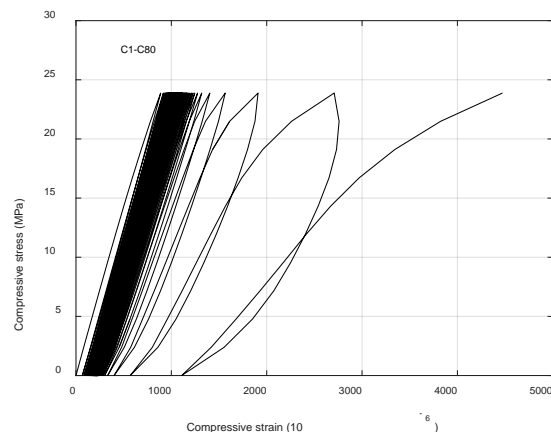
(b)

Fig. 8 The S-N diagrams of mortar for the simplified time-independent model, with Matsumoto et al.'s analysis [19] and Morris et al.'s data [29]. (a) Compression; (b) Tension

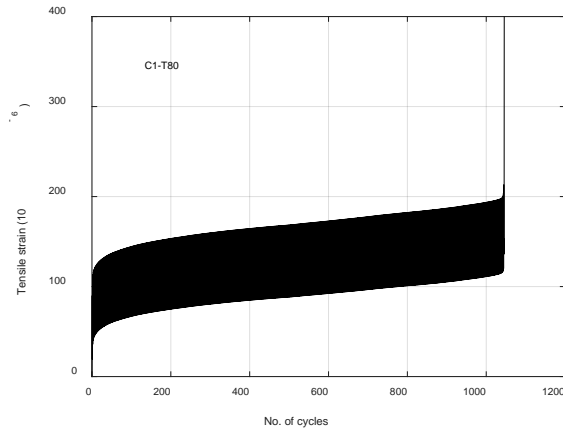
The fatigue life with different stress levels are shown in the S-N curve of mortar as presented in Fig. 8, and the simulation results are also compared with Matsumoto's analysis [19] and Morris et al.'s experimental data [29]. It can be seen that the simulation results of compressive fatigue agree well with Matsumoto's results and experimental data. While for the tensile fatigue modeling, the experimental data does not follow the common S-N curve, but with much smaller slope (Fig. 8 (b)). This might be due to the sensitivity problem when conducting the tension test. Nevertheless, for numerical simulation, the calibrated parameters should guarantee that the simulated S-N curve will generally go through the reference point, for which at the stress level of 1.0, the fatigue life would be 1.



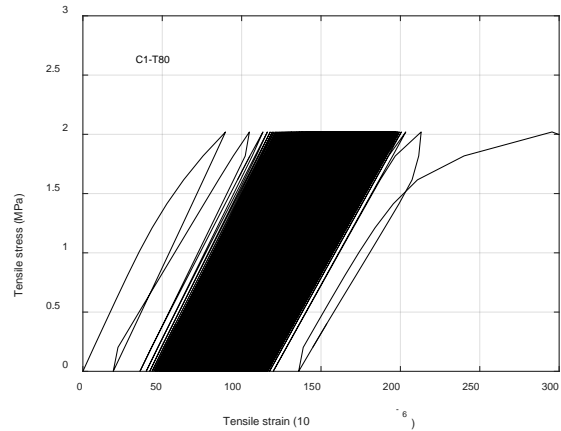
(a)



(b)

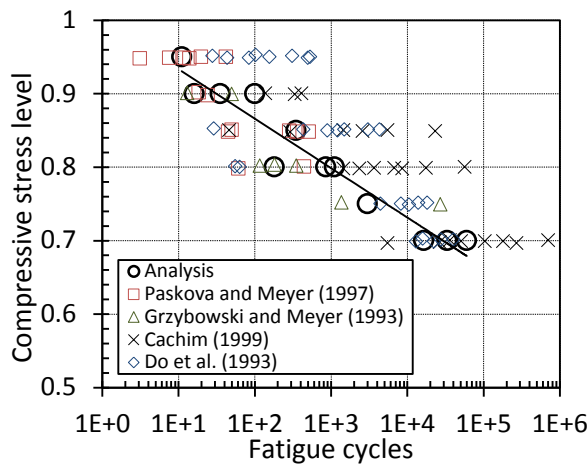


(c)

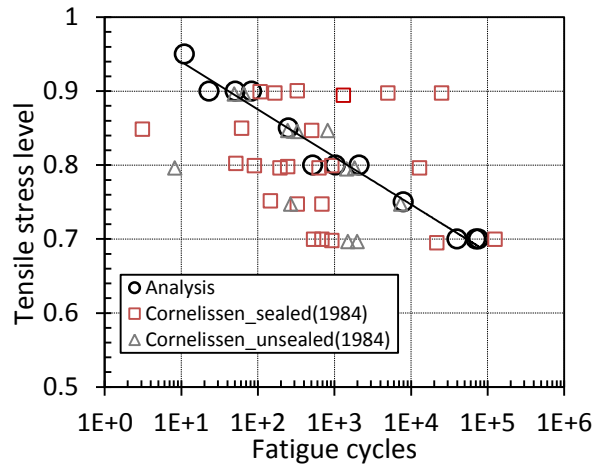


(d)

Fig. 9 The global strain history and the global stress-strain curves of concrete in compressive and tensile fatigue  
(a) Strain history in 80% compression (b) Stress-strain curve in 80% compression (c) Strain history in 80% tension (d) Stress-strain curve in 80% tension



(a)



(b)

Fig. 10 The simulated S-N curves of concrete (a) Compressive and tensile fatigue for concrete (b) Simulated compressive fatigue life with experiment data

Then by introducing the similar degradation process to the ITZ, the fatigue failure of concrete can be simulated. In Fig. 9, several cases are shown with the strain development and the stress-strain curves. It can be seen that for the compression fatigue, the cumulated residual deformation is still mainly coming from the creep but with smaller values due to the existence of coarse aggregates, whose creep can be neglected compared to cement mortar [30]. The tensile fatigue of concrete also becomes different compared to mortar, that is, although the increasing of the residual strain can be seen, the values are smaller compared to pure mortar. This phenomenon occurs because that, for the concrete under tensile stresses, the ITZ whose strength is much weaker

than the mortar part will have cracks first. As a result, during the most of the fatigue life, the damage cumulating will mainly occur in the ITZ, meanwhile the mortar part may still stay within the elastic region. Therefore, the global residual deformation could be smaller despite of the big crack opening in ITZ.

The S-N curves of the compressive and tensile fatigue for concrete are simulated, which can be seen in Fig. 10. The two simulated S-N curves have similar shape and tendency, and the fatigue lives are within the same range. The previous data are collected from the compressive and tensile fatigue tests for the comparison purpose. The compressive fatigue data are picked from Lee and Barr's review paper [31], and the original data are coming from several experiments [32-35], as shown in Fig. 10 (a). While for the tensile fatigue, Cornelissen's study [36] is referred, in which two kinds of curing conditions were used (sealed and open to air). Considering the big scatter in the fatigue experiments, the simulated S-N curves for concrete are within the range of previous data, and the slopes of S-N curves are also in a good agreement with the average values of previous experiments.

## 4.2 FTC damage and static strength

In order to introduce different levels of frost damage before analyzing the fatigue behavior, the free expansion during 300 FTCs has been simulated first, which corresponds to Hasan's FTC experiments [7]. The details of ice formation modeling, internal pressure modeling and environmental conditions can be found in literature [13]. Here only the simulated result of free FTC expansion is shown (Fig. 11) as the given initial condition for fatigue analysis. According to Hasan's discussion [7], and considering the nature of RBSM constitutive model, the residual tensile strain after each FTC is the most important parameter which can be linked to other material properties, such as the stiffness, strength and so on. Therefore, once the simulated residual strain matches the measured data, the FTC damage in experiments can be represented reasonably by the RBSM simulation.

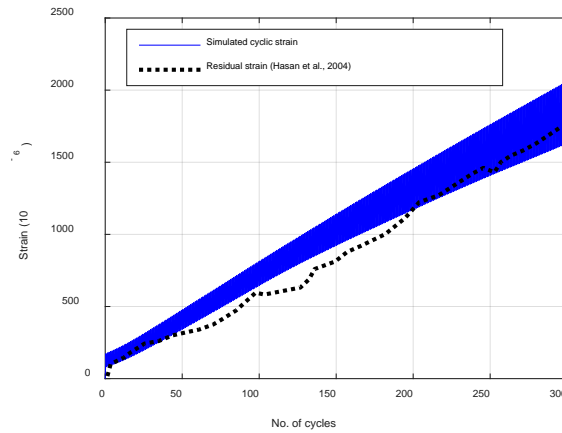


Fig. 11 Simulated cyclic strain and experimental measurements in 300 FTC

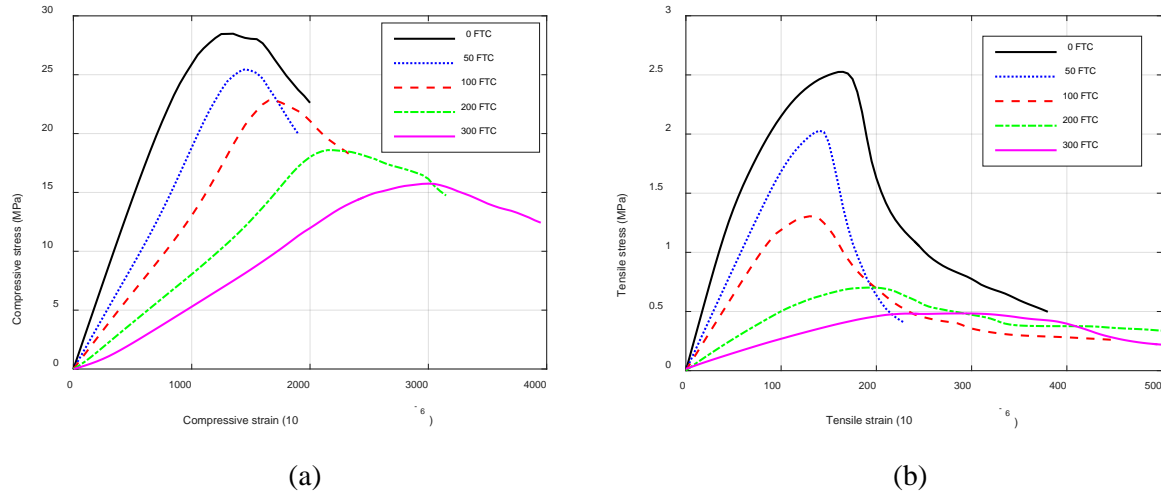


Fig. 12 The static strengths of concrete with different numbers of FTC (a) Compression (b) Tension

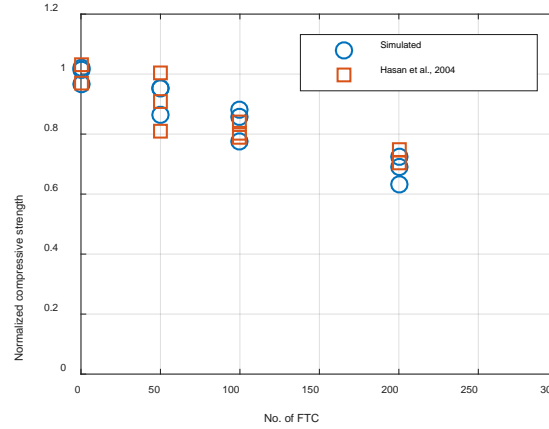
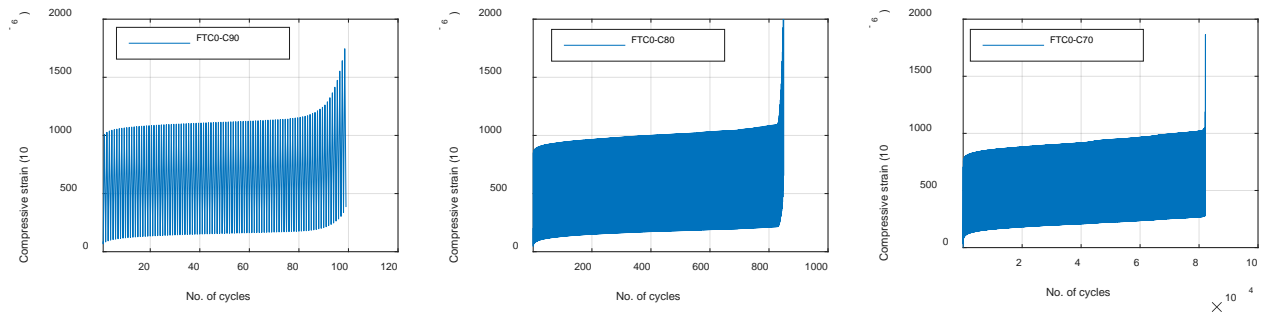


Fig. 13 Degradation of compressive strength after different numbers of FTC

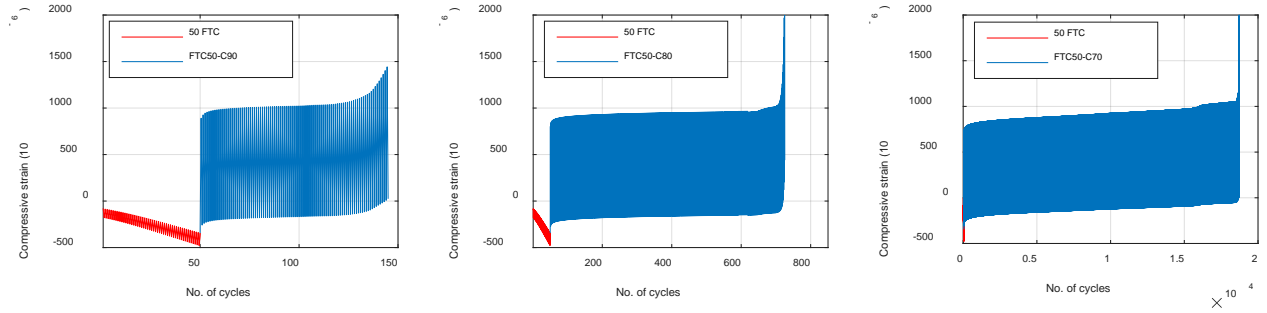
The static compressive and tensile behaviors after different numbers of FTCs are simulated and shown in Fig. 12. It can be seen that as the number of FTCs increases, both the residual stiffness and strengths decreases gradually, and at the meanwhile, both the ascending and softening parts become more ductile. Same phenomenon has also been reported in previous studies for compression [37] and tension [38]. The normalized reduction in compressive strength is compared with Hasan's experimental data [7] after different numbers of FTCs, as shown in Fig. 13. Although some variation is existed in both experimental and analytical data, the average values are still in a good agreement. Therefore, the FTC damage simulation and residual mechanical properties are reliable to be used in the following fatigue analysis.

### 4.3 Fatigue behavior after FTC damage

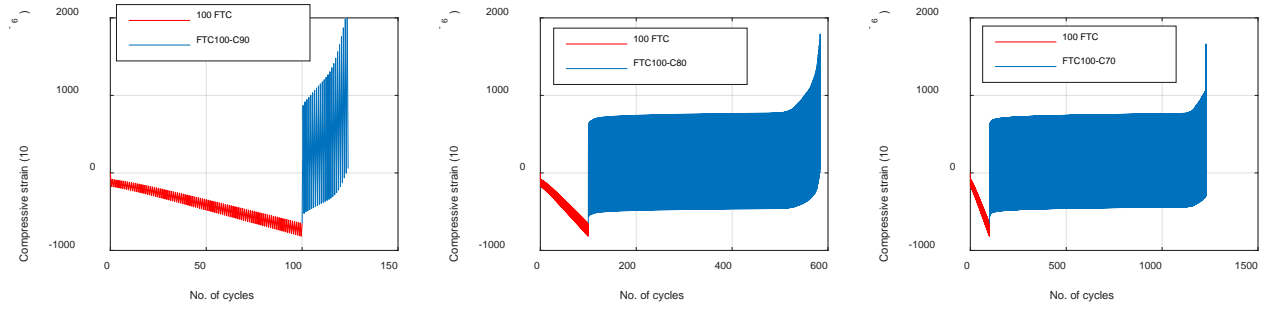
1



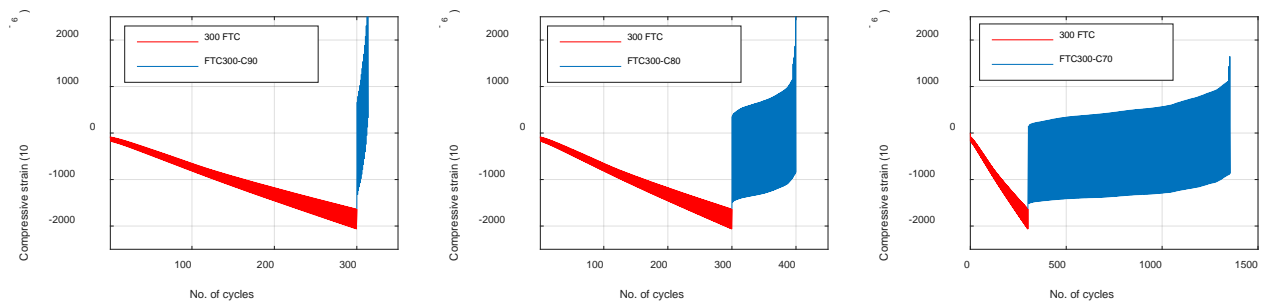
2



3



4



5

6

7

Fig. 14 Strain development under different numbers of FTC and followed by different levels of compressive fatigue stress

### Deformation $\times 10$

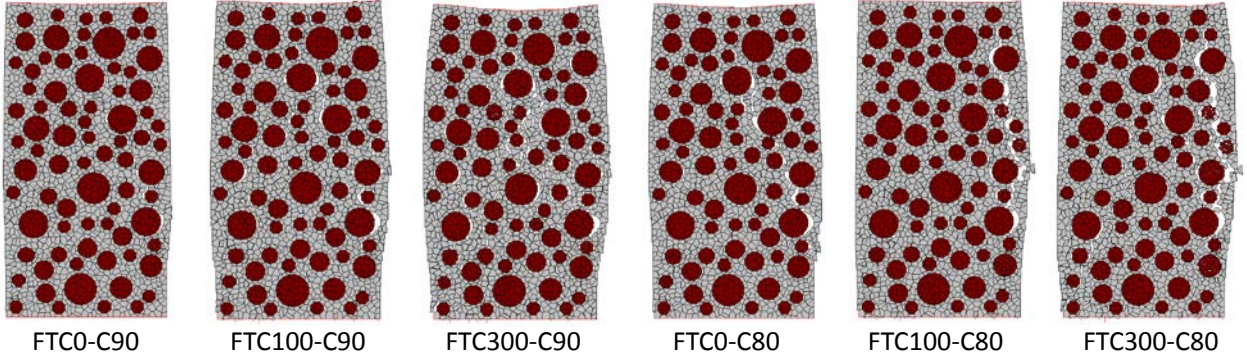


Fig. 15 Crack opening and failure mode of compressive fatigue after FTC damage

Using the FTC damaged concrete, and based on the residual strengths (used as stress level 1.0), the fatigue simulation is conducted. Fig. 14 shows the strain development under the combined FTCs and compressive fatigue cycles. The expansive freezing stress during FTCs will cause continuously increasing expansion, which is reflected as negative compressive strain (red curve in Fig. 14). When the FTC test stops, there is a residual expansion, and this residual deformation should be recovered first when the compressive loading is applied from the top of the concrete prism in the real experiments. For each compressive stress level, as the number of FTCs increases, the stiffness of material will decrease and the concrete will become more ductile, and thus, the strain amplitude during fatigue will increase. Although the bigger FTC damage means a smaller absolute compressive stress for each stress level, it will still result in a shorter fatigue life. In addition, once bigger FTC damage is introduced, the strain development at the very end of failure stage shows bigger ductility. Some examples of crack pattern and failure mode are shown in Fig. 15, in which the deformation has been enlarged by 10 times. For both 90% and 80% stress level, concrete with bigger FTC damage shows a more uniform crack distribution. This is because FTCs will generate many uniformly distributed mesoscale cracks, and these mesoscale cracks will prevent localized failure under fatigue loadings. Since not a single major crack, but many mesoscale cracks will develop and grow during the fatigue life, more energy will be absorbed so that the concrete could become more ductile (bigger strain development).

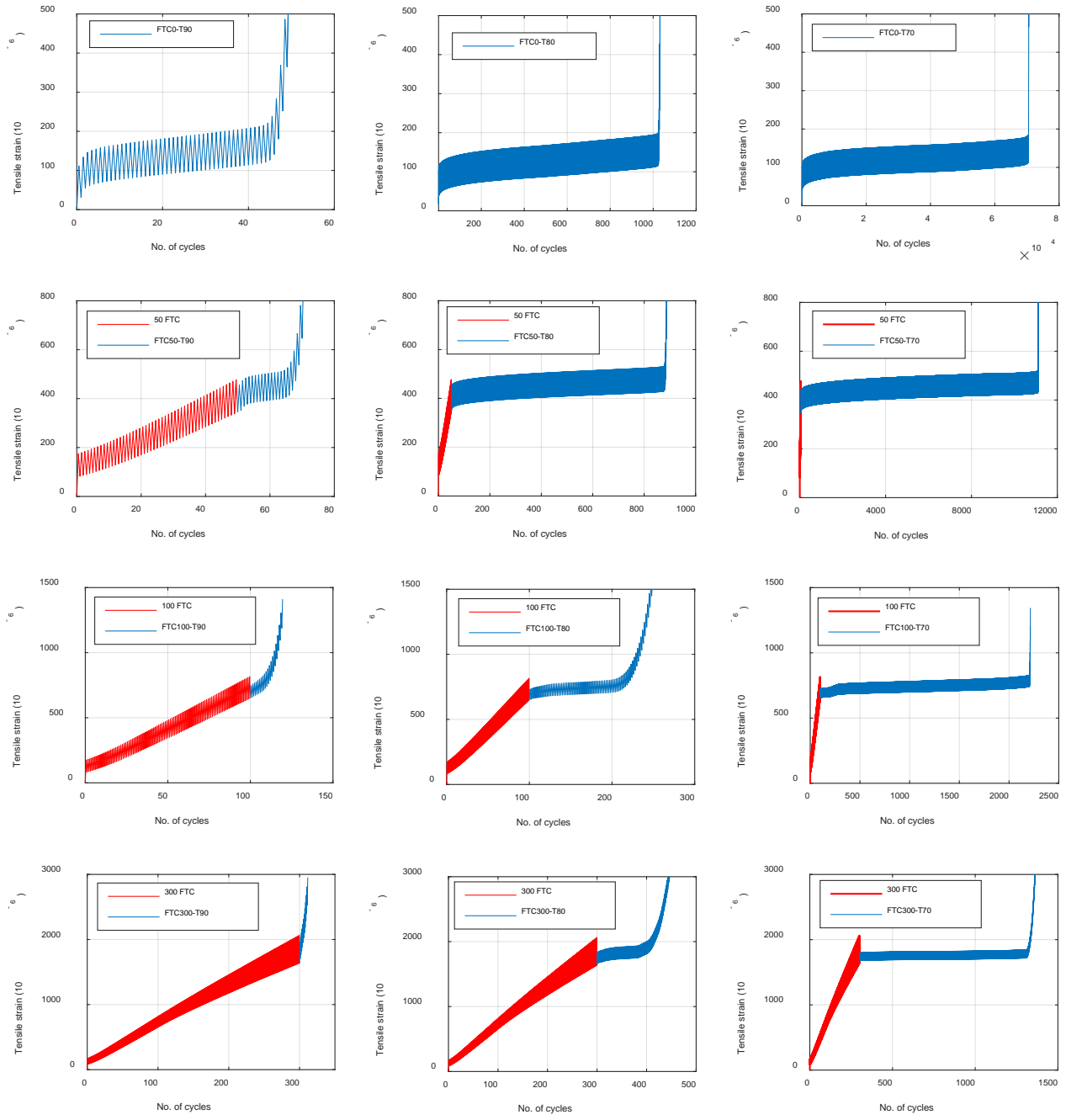


Fig. 16 Strain development under different numbers of FTC and followed by different levels of tensile fatigue stress



## Deformation $\times 50$

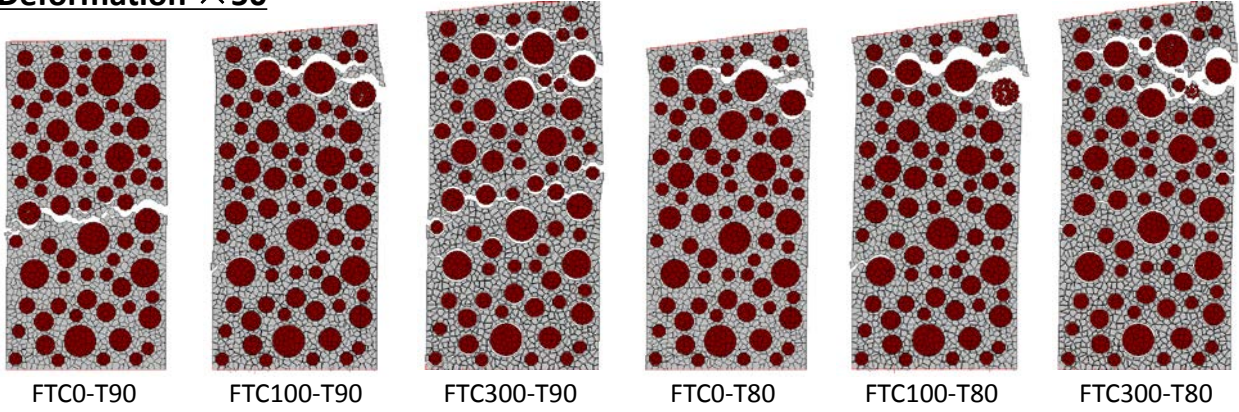


Fig. 17 Crack opening and failure mode of tensile fatigue after FTC damage

For the case of tensile fatigue, similar strain development curves of concrete with different FTC damage and different stress levels are shown in Fig. 16. Under this condition, the deformations in both FTCs and fatigue cycles are in the same direction. Similar with the compression fatigue, the tensile fatigue also shows a clear reduction in fatigue life if more numbers of FTCs were introduced. In addition, at each stress level, the deformation under fatigue also become more ductile if FTC damage is bigger. The failure modes are shown in Fig. 17, in which the deformation has been enlarged by 50 times. For the non-FTC damaged cases, only a single major crack is generated when tensile failure occurs because of the stress relaxation in the non-cracked elements. However, once more mesoscale cracks are introduced by FTCs, the stress relaxation effect would become much smaller. Therefore, even after one major crack is generated, cracks at other locations can still grow, thus in macroscale the concrete material will show a bigger ductility and a more uniform damage.

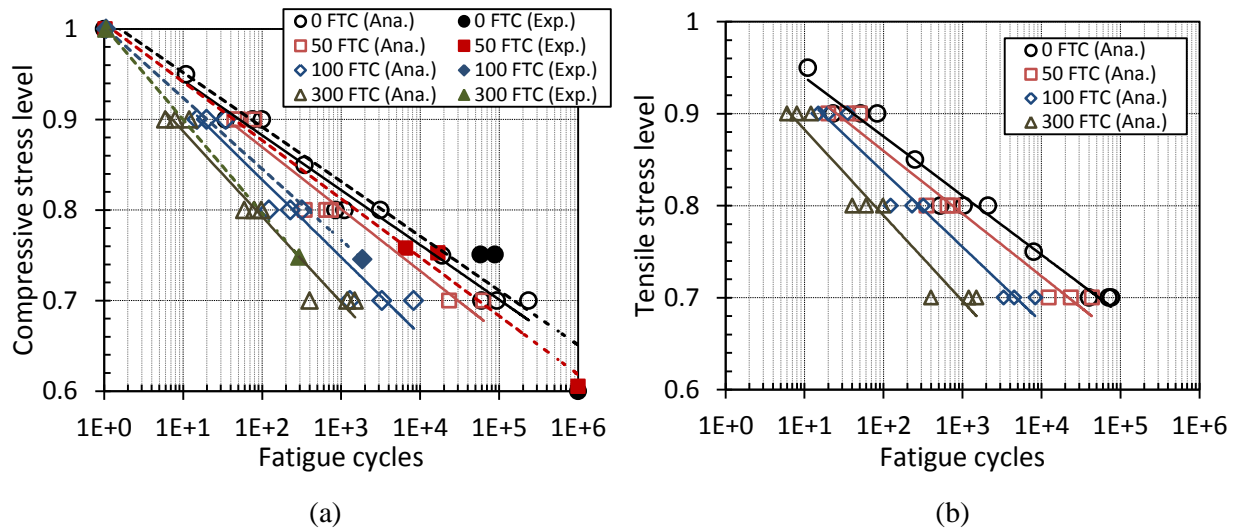


Fig. 18 S-N curves of compressive and tensile fatigue life for FTC damage concrete and undamaged concrete (experimental data of compressive fatigue comes from [9]) (a) Compression (b) Tension



The S-N curves in Fig. 18 show that the FTC damaged concrete will have a shorter fatigue life than the undamaged ones, and still a linear relationship can be regressed. Once expansive FTC damage is introduced before fatigue, most of the normal springs of mortar and ITZ will reach the softening part (the shear capacity also closely relies on the normal springs), then the damage cumulating during fatigue will become faster than undamaged concrete, therefore the fatigue life will become shorter. The simulated compressive fatigue life is compared with Hasan et al.'s data [9], and the reduction effects by different FTCs are in a good agreement between the analytical and experimental results.

## 5. Conclusions

In this paper, the mesoscale numerical approach based on RBSM has been developed for the combined FTCs and mechanical fatigue problem. The simulated results show a good agreement with previous experimental data. The detailed conclusions are:

- (1) The constitutive laws under fatigue loading are developed and discussed. The degradation caused by cyclic loading is introduced and formulated for the normal and shear springs of mortar and ITZ, and finally combined with the fatigue creep model in a simpler way. The simulated fatigue behaviors of non-FTC damaged mortar and concrete show a good agreement with common knowledge and previous experimental data.
- (2) The internal stress model induced by FTCs is combined with the cyclic constitutive laws to simulate the fatigue behavior after different levels of FTC damage. First in the simulation, different numbers of FTCs are applied to obtain different frost damage levels. Then using the FTC damaged concrete, static test is simulated to obtain the residual compressive and tensile strengths. The simulation results show that both the static stiffness and strengths will decrease proportionally to the FTC-induced irreversible tensile strain. And the stress strain relationship of damaged material will become more ductile in both ascending and softening stages. The simulated static performance agrees with experimental phenomenon well.
- (3) Finally, the fatigue behaviors of concrete are simulated for different levels of FTC damage. The residual static strengths calculated above are used as the new reference strengths in fatigue simulation. Although the absolute stresses applied on FTC damaged concrete is smaller than non-damaged ones, the fatigue life still shows a significant reduction, as reported in pervious experiments. During the fatigue simulation, the FTC damaged concrete shows a more ductile performance due to the pre-introduced mesoscale cracks. The S-N curve for the FTC damaged concrete still follows a linear relationship.

(4) In this simulation, the fatigue test is conducted after FTC damage in room temperature, and shows a clear decreasing in fatigue life. However, some experiments under simultaneous FTCs and mechanical fatigue showed a longer life than the single effect. When ice exists in pores, concrete material will be strengthened so that the fatigue damage could become smaller. The mechanism and numerical simulation under this condition should be investigated in the future. In addition, the 2D model presented in this paper will also be extended to the 3D case in the future studies.

## Acknowledgement

The authors would like to express their sincere thanks to the Grant-in-Aid for Scientific Research (A) of Japan Society of Promotion of Science (No. 26249064). The first author would also like to express his sincere thanks to the JSPS (Japan Society of Promotion of Science) Fellowship (D2-PD) for the research work.

## Appendix A. Mathematical bases of RBSM

The RBSM was firstly developed by Kawai [18], together with its theoretical bases. The current 2D computer program used in this study is based on Nagai's work [39], and for the Voronoi meshing, the geometric computational software developed by Sugihara [40] is applied.

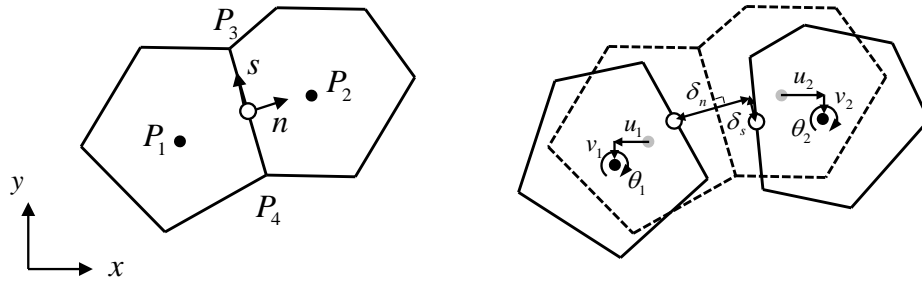


Fig. 19 Local displacement of elements [39]

The elongation of the springs at normal and shear directions ( $\delta_n$ ,  $\delta_s$ ) is calculated from the relative deformation of the midpoints ( $x_f$ ,  $y_f$ ) at the shared face. Then the relative displacement [ $u_1$ ,  $v_1$ ,  $\theta_1$ ] of Element 1 to the midpoint ( $x_f$ ,  $y_f$ ) is:

$$\begin{aligned} u &= u_1 - (y_f - y_1)\theta_1 \\ v &= v_1 + (x_f - x_1)\theta_1 \end{aligned} \quad (36)$$

The same equations can be applied to Element 2, then ( $\delta_n$ ,  $\delta_s$ ) can be known. The transformation from  $x$ - $y$  to  $n$ - $s$  coordination is:

$$\mathbf{d} = \mathbf{B}\mathbf{u}_e \quad (37)$$

1 where  $\mathbf{d}^T = [\delta_n, \delta_s]$  and  $\mathbf{u}_e^T = [u_1, v_1, \theta_1, u_2, v_2, \theta_2]$ . The transformation matrix  $\mathbf{B}$  is:

$$2 \quad \mathbf{B} = \frac{1}{l_{43}} \begin{bmatrix} y_{43} & -x_{43} & (-x_{43}x_{p1} - y_{43}y_{p1}) & -y_{43} & x_{43} & (x_{43}x_{p2} + y_{43}y_{p2}) \\ x_{43} & y_{43} & (y_{43}x_{p1} - x_{43}y_{p1}) & -x_{43} & -y_{43} & (-y_{43}x_{p2} + x_{43}y_{p2}) \end{bmatrix} \quad (38)$$

3 where  $x_{ij} = x_i - x_j$ ,  $y_{ij} = y_i - y_j$  and  $l_{43}$  means the length of the shared boundary. In addition,

$$4 \quad \begin{aligned} x_{pi} &= (x_{4i} + x_{3i}) / 2 \quad (i = 1, 2) \\ y_{pi} &= (y_{4i} + y_{3i}) / 2 \quad (i = 1, 2) \end{aligned} \quad (39)$$

5 Then the local equilibrium can be expressed in global coordinate as:

$$6 \quad \mathbf{k}_e \Delta \mathbf{u}_e = \Delta \mathbf{f}_e \quad (40)$$

7 where the element stiffness matrix associated with the shared boundary ( $\mathbf{k}_e$ ) is:

$$8 \quad \mathbf{k}_e = \mathbf{B}^T \mathbf{D} \mathbf{B} \quad (41)$$

9 where

$$10 \quad \mathbf{D} = \begin{bmatrix} k_n & 0 \\ 0 & k_s \end{bmatrix} \quad (42)$$

11

## 12 **Appendix B. Mesh convergence of RBSM**

13 The iteration process of the current program adopts the modified Newton-Raphson method due to the negative  
14 stiffness in the tension softening part. Actually, the poor efficiency in iteration can be also lessened by the smaller  
15 size of total matrix in RBSM, because there are only three degrees of freedom in each element, which is much less  
16 than the FEM. The convergence criterion is as follows:

$$17 \quad \frac{\|\Delta F\|}{\|R\|} \leq 10^{-4} \quad (43)$$

18 where  $\Delta F$  is the unbalanced nodal force and  $R$  is the loading and reaction forces. In the RBSM analysis, large  
19 deformation is allowed and the two elements can be totally separated without any stress transfer. Therefore, the  
20 convergence will be much slower after failure happens, and Eq. (43) may not be reached. In this case, the fixed  
21 maximum iteration number has been set manually, so that the program can still go to the next step.

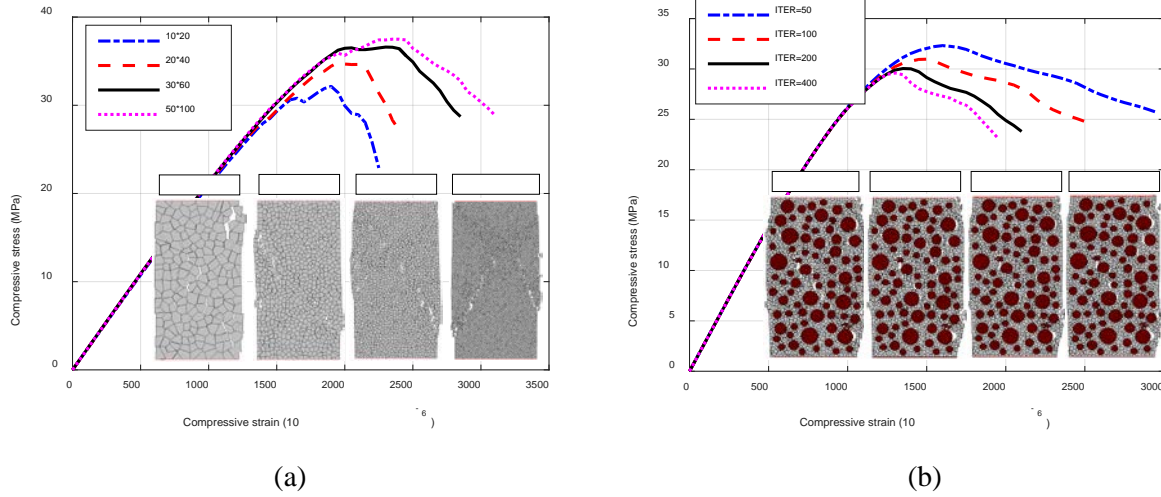


Fig. 20 Sensitivity of the mesh size and maximum iteration number (a) effect of mesh size on compression of mortar (b) effect of iteration number on compression of concrete

Fig. 20 shows the effects of mesh size and maximum iteration number on simulation results. The convergence in tension tests is much faster than the compression tests due to the weak coupling between normal and shear springs, thus here only the compression cases are discussed. Too big mesh size will lead to a significant bias error from the real solution (Fig. 20 (a)) and even the failure mode may not be accurate. Considering the balance between computation time and accuracy, for a prism (100×100×200 mm) mesh with size of 3.3mm (namely 30×60 mesh) can provide the acceptable accuracy and also the mesh size dependency can be largely reduced. Another factor is the maximum iteration number after big tensile and shear failure occurs, and from Fig. 20 (b), 200 iteration steps can be enough for an acceptable accuracy. Actually, the smaller mesh is, the higher efficiency the iteration has. It can also be seen that the convergence level will affect the softening branch but has little effects on the failure mode.

## References

- [1] Fagerlund, G. (2002). "Mechanical damage and fatigue effects associated with freeze-thaw of materials." M. J. Setzer, R. Auberg and H. J. Keck. Eds. *Proc. 2<sup>nd</sup> International RILSM Workshop on Frost Resistant of Concrete*, Essen 18-19 April 2002. Cachan Cedex: RILEM Publications S.A.R.L., 117-132.
- [2] Powers, T. C (1945). "A working hypothesis for further studies of frost resistance of concrete." *Proc., ACI journal Proceedings*, ACI. Vol. 41, No. 1, pp. 245-272
- [3] Scherer, G. W., and Valenza II, J. J. (2005). "Mechanisms of frost damage." *Materials science of concrete*, 7, 209-246.

- [4] Coussy, O., (2005). "Poromechanics of freezing materials." *Journal of the Mechanics and Physics of Solids*, 53, 1689-1718.
- [5] Coussy, O. and Monteiro, P.J.M., (2009), "Errata to "Poroelastic model for concrete exposed to freezing temperatures" [Cement and Concrete Research 38 40-48]", *Cement and Concrete Research*, 39, 371-372.
- [6] Gong, F., Sicat, E., Zhang, D., and Ueda, T. (2015a). "Stress Analysis for Concrete Materials under Multiple Freeze-Thaw Cycles." *Journal of Advanced Concrete Technology*, 13(3), 124-134.
- [7] Hasan, M., Okuyama, H., Sato, Y., and Ueda, T. (2004). "Stress-strain model of concrete damaged by freezing and thawing cycles." *Journal of Advanced Concrete Technology*, 2(1), 89-99.
- [8] Gong, F., Sicat, E., Ueda, T., and Zhang, D. (2013). "Meso-scale Mechanical Model for Mortar Deformation under Freeze Thaw Cycles." *Journal of Advanced Concrete Technology*, 11(2), 49-60.
- [9] Hasan, M., Ueda, T., and Sato, Y. (2008). "Stress-strain relationship of frost-damaged concrete subjected to fatigue loading." *Journal of Materials in Civil Engineering*, 20(1), 37-45.
- [10] Nagai, K., Sato, Y., and Ueda, T. (2004). "Mesoscopic simulation of failure of mortar and concrete by 2D RBMSM." *Journal of Advanced Concrete Technology*, 2(3), 359-374.
- [11] Ueda, T., Hasan, M., Nagai, K., Sato, Y., and Wang, L. (2009). "Mesoscale simulation of influence of frost damage on mechanical properties of concrete." *Journal of Materials in Civil Engineering*, 21(6), 244-252.
- [12] Matsumoto, K., Sato, Y., Ueda, T., and Wang, L. (2008). "Mesoscopic analysis of mortar under high-stress creep and low-cycle fatigue loading." *Journal of Advanced Concrete Technology*, 6(2), 337-352.
- [13] Gong, F., Wang, Y., Zhang, D., and Ueda, T. (2015b). "Mesoscale Simulation of Deformation for Mortar and Concrete under Cyclic Freezing and Thawing Stress." *Journal of Advanced Concrete Technology*, 13(6), 291-304.
- [14] Wang, L., Soda, M., and Ueda, T. (2008). "Simulation of chloride diffusivity for cracked concrete based on RBMSM and truss network model." *Journal of Advanced Concrete Technology*, 6(1), 143-155.
- [15] Wang, L., and Ueda, T. (2011). "Mesoscale modeling of water penetration into concrete by capillary absorption." *Ocean Engineering*, 38(4), 519-528.
- [16] Wriggers, P., and Moftah, S. (2006). "Mesoscale models for concrete: Homogenisation and damage behaviour." *Finite elements in analysis and design*, 42(7), 623-636.
- [17] Wang, X., Zhang, M., and Jivkov, A. P. (2015). "Computational technology for analysis of 3D meso-structure effects on damage and failure of concrete." *International Journal of Solids & Structures*, 80, 310-333.
- [18] Kawai, T., (1977). "New element models in discrete structure analysis." *Journal of Society of Naval Architectures of Japan*, 141, 187-193.
- [19] Matsumoto, K., Sato, Y., and Ueda, T. (2010). "Fracture mechanism and prediction of deformation of mortar under time-dependent loads by meso-scale analysis." *Doboku Gakkai Ronbunshuu E/JSCE Journal of Materials, Concrete Structures and Pavements*, 66(4), 380-398. (In Japanese)

- 1 [20] Sicat, E., Gong, F., Zhang, D., and Ueda, T. (2013). "Change of the Coefficient of Thermal Expansion of  
2 Mortar Due to Damage by Freeze Thaw Cycles." *Journal of Advanced Concrete Technology*, 11(12), 333-346.
- 3 [21] Sicat, E., Gong, F., Ueda, T., and Zhang, D. (2014). "Experimental investigation of the deformational  
4 behavior of the interfacial transition zone (ITZ) in concrete during freezing and thawing cycles." *Construction  
5 and Building Materials*, 65, 122-131.
- 6 [22] Bazant, Z. P., and Baweja, S. (2000). "Creep and shrinkage prediction model for analysis and design of  
7 concrete structures: Model B3." *ACI Special Publications*, 194, 1-84.
- 8 [23] Bazant, Z. P., and Hubler, M. H. (2014). "Theory of cyclic creep of concrete based on Paris law for fatigue  
9 growth of subcritical microcracks." *Journal of the Mechanics and Physics of Solids*, 63, 187-200.
- 10 [24] Neville, A. M. (1970). *Creep of concrete*. North-Holland Publishing Co.
- 11 [25] Neville, A. M. (1995). *Properties of concrete*. 4<sup>th</sup> edition, John Wiley & Sons, Inc.
- 12 [26] Gong, F., Zhang, D., Sicat, E., and Ueda, T. (2014). "Empirical estimation of pore size distribution in cement,  
13 mortar, and concrete." *Journal of Materials in Civil Engineering*, 26(7).
- 14 [27] Sun, Z., and Scherer, G. W. (2010). "Effect of air voids on salt scaling and internal freezing." *Cement and  
15 Concrete Research*, 40(2), 260-270.
- 16 [28] JSCE. (2005). "Standard specification for concrete structures – 2002 'material and construction' 6.2.5.3  
17 grading." *JSCE guidelines for concrete, No. 6, Japan Society of Civil Engineers*.
- 18 [29] Morris, A., and Garrett, G. (1981). "A comparative study of the static and fatigue behaviour of plain and steel  
19 fibre reinforced mortar in compression and direct tension." *International Journal of Cement Composites and  
20 Lightweight Concrete*, 3(2), 73-91.
- 21 [30] Bazant, Z. P., and Wittmann, F. H. (1982). "Creep and shrinkage in concrete structures." *John Wiley & Sons*
- 22 [31] Lee, M., and Barr, B. (2004). "An overview of the fatigue behaviour of plain and fibre reinforced concrete."  
23 *Cement and Concrete Composites*, 26(4), 299-305.
- 24 [32] Paskova, T., and Meyer, C. (1997). "Low-cycle fatigue of plain and fiber-reinforced concrete." *ACI  
25 Materials Journal*, 94(4).
- 26 [33] Grzybowski, M., and Meyer, C. (1993). "Damage accumulation in concrete with and without fiber  
27 reinforcement." *ACI Materials Journal*, 90(6).
- 28 [34] Cachim, P. B. (1999). "Experimental and numerical analysis of the behaviour of structural concrete under  
29 fatigue loading with applications to concrete pavements." PhD thesis, Faculty of Engineering of the University  
30 of Porto, p. 246.
- 31 [35] Do, M.-T., Chaallal, O., and Aïtcin, P.-C. (1993). "Fatigue behavior of high-performance concrete." *Journal  
32 of Materials in civil Engineering*, 5(1), 96-111.
- 33 [36] Cornelissen, H. (1984). "Fatigue failure of concrete in tension." *HERON*, 29 (4), 1984.

- 1 [37] Duan, A., Jin, W., and Qian, J. (2011). "Effect of freeze–thaw cycles on the stress–strain curves of  
2 unconfined and confined concrete." *Materials and structures*, 44(7), 1309-1324.
- 3 [38] Yang, Z. (2004). "Assessing cumulative damage in concrete and quantifying its influence on life cycle  
4 performance modeling." PhD Thesis, Purdue University.
- 5 [39] Nagai, K. (2005). "Mesoscopic Simulation of Failure of Mortar and Concrete by RBSM", PhD Thesis,  
6 Hokkaido University
- 7 [40] Sugihara, K. (1998). "Fortran Computational Geometry Programming." Tokyo: Iwanami Shorten (in  
8 Japanese)